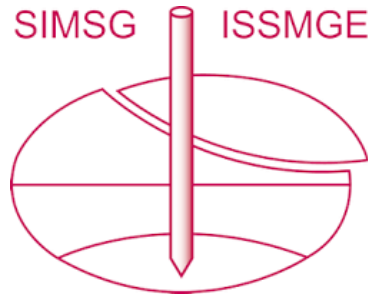


INTERNATIONAL SOCIETY FOR SOIL MECHANICS AND GEOTECHNICAL ENGINEERING



This paper was downloaded from the Online Library of the International Society for Soil Mechanics and Geotechnical Engineering (ISSMGE). The library is available here:

<https://www.issmge.org/publications/online-library>

This is an open-access database that archives thousands of papers published under the Auspices of the ISSMGE and maintained by the Innovation and Development Committee of ISSMGE.

The paper was published in the proceedings of the 10th European Conference on Numerical Methods in Geotechnical Engineering and was edited by Lidija Zdravkovic, Stavroula Kontoe, Aikaterini Tsiampousi and David Taborda. The conference was held from June 26th to June 28th 2023 at the Imperial College London, United Kingdom.

To see the complete list of papers in the proceedings visit the link below:

<https://issmge.org/files/NUMGE2023-Preface.pdf>

Constitutive model with reversal surfaces for granular soils under monotonic and cyclic loading

T.G. Limnaiou^{1,2} and A.G. Papadimitriou²

¹*GR8 GEO, Engineering consultants, Athens, Greece*

²*National Technical University of Athens, Athens, Greece*

ABSTRACT: This paper outlines the formulation and verification of a new constitutive model, named *LiPa* model, that simulates the monotonic and cyclic shearing of granular soils with the same set of soil-specific model constants. It is a SANISAND-type model and employs the last stress reversal point for defining both the elastic and the plastic strain rates. The updating of this point is specially treated to mitigate stress-strain overshooting. Macroscopic sand fabric evolution indices that scale the plastic modulus and dilatancy functions are incorporated, targeting accurate strain accumulation with cycles during shearing, both before and after liquefaction. Model performance is verified against sand-specific monotonic and cyclic shearing tests on Toyoura sand, while the validation is complemented with comparisons against empirical relations targeting generic aspects of the cyclic response: small - strain shear modulus degradation and hysteretic damping increase, volumetric and shear strain accumulation with cycles, effect of stress level on liquefaction resistance. A variety of loading conditions is included in the verification process, i.e., drained/undrained, monotonic/cyclic, to demonstrate the simulative potential of the model. It is shown that a single set of soil-specific constants may be used for both monotonic and cyclic shearing of any strain level, irrespective of stress level and relative density.

Keywords: Constitutive modeling, Cyclic loading, Monotonic loading, Liquefaction, Granular materials

1 INTRODUCTION

The accuracy of numerical analyses of geotechnical structures relies, among others, on the use of properly calibrated constitutive models that are appropriate for the examined geomaterial and loading conditions. For granular soils (e.g., sands or gravels), it is common that different constitutive models and/or different calibrations of the same model are employed, based on the initial conditions (e.g., density, stress level) and the target loading (monotonic vs cyclic, drained vs undrained).

For cyclic loading of granular soils, multiple constitutive models have been proposed. In many cases, the publications of such models include accurate simulations of monotonic loading and few (hand-picked) cyclic loading test comparisons focusing on liquefaction. However, such a presentation may not be sufficient for the whole spectrum of cyclic loading, which is highly dependent on cyclic shear strain level, from: a) the small-strain (“elastic”) response, to b) the medium-strain response (shear modulus degradation and accumulation of strains with cycles) and reaching: c) the large-strain response, mostly related to liquefaction. On the other hand, some of the models that have been accurately validated for cyclic loading, may not be as accurate when it comes to monotonic loading, or need different calibration to exhibit a satisfactory response.

Considering all the above, a new general-purpose

constitutive model named *LiPa* (after the surnames of the authors) is presented, that targets both the monotonic (until the critical state) and the cyclic response (for any shear strain level) with a unique set of soil-specific constants for any relative density and stress level. It is a SANISAND-type model, i.e., it is a bounding surface model adopting the dependence of model surfaces on the state parameter ψ (Been and Jefferies, 1985), a notion first introduced by Manzari and Dafalias (1997). It does not have a small yield surface (e.g., Dafalias and Manzari 2004), but incorporates the concept of stress reversal surfaces (e.g., Papadimitriou et al., 2019) for proper simulation of cyclic loading. It builds on the NTUA-SAND model (Andrianopoulos et al., 2010), from which it inherits concepts like the small and medium-strain nonlinearity and the fabric evolution index for large strain response, both properly modified.

This paper presents a brief description of the key components of the *LiPa* model’s formulation (focusing on its novel ingredients) and in the sequel its validation against monotonic and cyclic data for two granular soils: one sand and one gravel. The (companion) paper of Limnaiou and Papadimitriou (2023b) presents this model’s validation against data from dynamic centrifuge tests in liquefaction problems.

2 KEY CONSTITUTIVE INGREDIENTS

The complete constitutive formulation of the *LiPa* constitutive model for granular soils is described in detail in Limnaiou and Papadimitriou (2023a). Due to length limitations, in this paper, only the key constitutive ingredients are outlined and explained. All constitutive equations refer to the multiaxial stress space. Second-order tensors are written in bold characters, to be distinguished from scalars (in plain), while normal stress components are considered effective. Symbol tr between two tensors denotes the trace (tr) of their product.

The role of stress ratio tensor $\mathbf{r} = \mathbf{s}/p$ (where p is the mean effective stress and \mathbf{s} is the deviatoric component of the effective stress tensor $\boldsymbol{\sigma}$) is instrumental in its equations. This because it is a stress-ratio driven model, i.e., a non-zero deviatoric stress-ratio rate is a necessary (but not sufficient) condition for non-zero plastic strain rates. Being a SANISAND-type model, it incorporates three surfaces in the stress space: the bounding, the dilatancy and the critical state surface, that take the form of homologous open cone surfaces with apex at the stress origin. A schematic illustration of these surfaces on the π -plane of the deviatoric stress ratio space is depicted on Figure 1. Their aperture depends on the Lode angle θ and the state parameter ψ (Been and Jefferies, 1985). The concept of stress reversal surfaces is introduced via updating tensor \mathbf{r}_{ini} that refers to the value of tensor \mathbf{r} at the initialization of a new stress path after a load reversal and it is used in many aspects of the model. Firstly, as shown in Figure 1 it is used in the mapping rule that pinpoints the image stress ratio on the bounding surface (\mathbf{r}^{b}) and, through it, the unit-norm deviatoric direction (\mathbf{n}) of the plastic strain rate and the image stress ratios on the dilatancy and the critical state surfaces, \mathbf{r}^{d} and \mathbf{r}^{c} respectively.

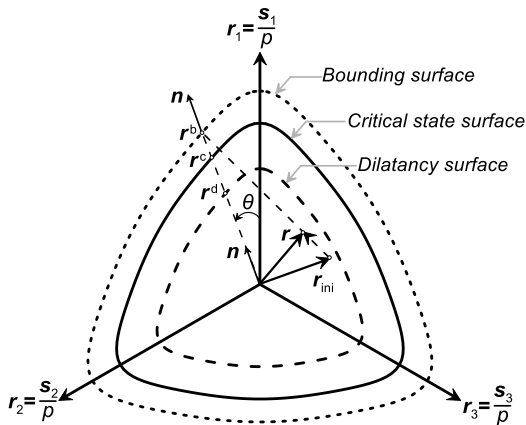


Figure 1. Model surfaces on the π -plane of the deviatoric stress ratio space and adopted mapping rule.

The model incorporates a vanished yield surface and the elastic shear modulus (G_t) is a function of the current values of mean effective stress p and the void ratio e ,

following a Ramberg-Osgood non-linear formulation:

$$G_t = \frac{G_{\max}}{T} = \frac{G_o p_{\text{atm}} \left(\frac{1}{0.3 + 0.7e^2} \right) \sqrt{\frac{p}{p_{\text{atm}}}}}{T} \quad (1)$$

where G_o is a model constant, p_{atm} is the atmospheric pressure and T is a scalar variable defined as:

$$T = 1 + 2 \left(\frac{1}{a_1} - 1 \right) \left(\frac{\sqrt{\frac{1}{2}(\mathbf{r} - \mathbf{r}_{\text{ini}}) : (\mathbf{r} - \mathbf{r}_{\text{ini}})}}}{a_1 \left(\frac{G_{\max}}{p} \right)^{\gamma_1}} \right) \geq 1 \quad (2)$$

where $a_1 = 0.85$ and $\gamma_1 = 0.0003$ are appropriate values for all granular soils. Note that these were considered model constants requiring calibration in the NTUA-SAND model from which Equations 1 and 2 were adopted. The elastic bulk modulus K_t is related to its shear counterpart G_t via a constant value, ν , of the Poisson's ratio (a model constant).

For the plastic strain rate, the scalar-valued plastic modulus K_p reads:

$$K_p = h_o h_f f_A(p, e, \theta) \frac{(\mathbf{r}^{\text{b}} - \mathbf{r}) : \mathbf{n}}{(\mathbf{r} - \mathbf{r}_{\text{ini}}) : \mathbf{n}} \quad (3)$$

where h_o is a nonnegative model parameter, h_f a nonnegative model fabric-function described in the sequel and f_A is a summary presentation of a product of functions that account for the effects of mean effective stress p , the void ratio e and the Lode angle θ . K_p is defined in terms of the distance of the current deviatoric stress ratio (\mathbf{r}) from its image point on the bounding surface (\mathbf{r}^{b}) as projected along the direction of \mathbf{n} . Its additional dependence on the distance of stress ratio (\mathbf{r}) from \mathbf{r}_{ini} (again projected on \mathbf{n}) ensures zero plastic strain rate at the initiation of loading following a load reversal. The scalar-valued function h_f describes macroscopically the effects of fabric evolution on the plastic modulus as:

$$h_f = \frac{1 + \langle f_p - c_f \rangle^2}{1 + \langle \mathbf{f}_{\text{ini}} : \mathbf{n} \rangle} \quad (4)$$

where $c_f = 1$ is a fixed model constant. The numerator of h_f is a quadratic function of scalar-valued variable f_p , in Macauley brackets. The denominator is a linear function of the inner product of an expression of the loading direction \mathbf{n} and the evolving fabric tensor \mathbf{f} , as captured at load reversal (thus the index ini), again in Macauley brackets. Both f_p and \mathbf{f} initiate from zero at the initial state (e.g., geostatic state) and evolve independently with the plastic volumetric strain rate, with the \mathbf{f} evolving only in dilation, due to the Macauley brackets:

$$\dot{f}_p = (2 - a) N(N_o, e_o, \psi_o) f_B(p_o) \dot{\varepsilon}_{\text{vol}}^{\text{p}} \quad (5)$$

$$\dot{\mathbf{f}} = -N(N_o, e_o, p_o) h_{\text{post-liq}} \left[\mathbf{f} + f_{\max}^{(1+a)} \mathbf{n} \right] \langle -\dot{\varepsilon}_{\text{vol}}^{\text{p}} \rangle \quad (6)$$

The nonnegative function N serves as a common evolution rate of both f_p and f , that depends on the calibration constant N_0 and the initial state in terms of p_0 and e_0 . The rate equation of f also includes function $h_{\text{post-liq}} (\geq 1)$, which is activated after the occurrence of initial liquefaction (discussed below). The gradual increase of the numerator of h_f with positive plastic volumetric strain provides a continuous increase of the K_p (stiffening) during successive loading-unloading cycles of small amplitude. Concurrently, the gradual increase of the denominator of h_f with negative plastic volumetric strain simulates the intensely compliant response after a large-amplitude cycle in undrained conditions, thus leading to initial liquefaction. The above operation of the denominator of h_f is perfectly appropriate for undrained conditions, but may lead to an unrealistic reduction of the stiffness under extensive loading under drained conditions (e.g., see Figure 2a).

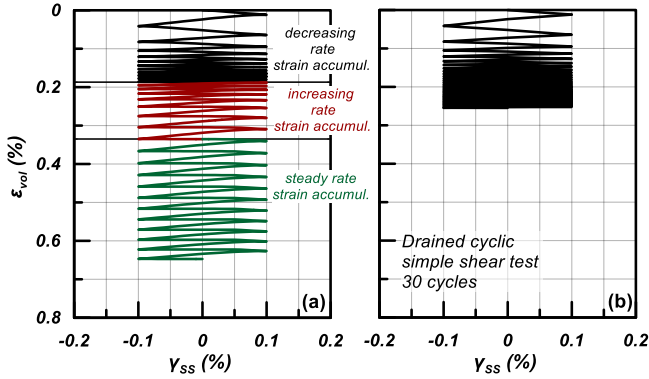


Figure 2. Volumetric strain accumulation during a strain-controlled simple shear test with factor a : (a) constant and equal to 1 and (b) varying according to Equation (7)

To counterbalance this effect, factor a (in Equations 5 and 6) is introduced:

$$0 \leq a = -2 \left(\frac{\int |\dot{\epsilon}_{\text{vol}}|}{\int \dot{\epsilon}_{\text{vol}}^p} - 1 \right) \leq 1 \quad (7)$$

Factor a varies linearly between 0 (fully drained conditions) and 1 (fully undrained conditions), depending on the ratio of the accumulated total volumetric strain over that of the plastic component and ensures a continuous stiffening under drained conditions (Figure 2b).

The present model adopts a non-associative flow rule and the plastic volumetric strain is estimated with the introduction of a scalar-valued dilatancy function, D . The dilatancy function acquires different forms for contraction and dilation, but both give $D = 0$, when the stress point is on the dilatancy surface (when $\mathbf{r} = \mathbf{r}^d$ in Figure 1). During contraction, the D is based on Rowe's dilatancy theory, but is also correlated to the (recent) shearing history (via \mathbf{r}_{ini}) as follows:

$$D = A_0 \frac{f_B((\mathbf{r} - \mathbf{r}_{\text{ini}}) : \mathbf{n})}{f_C(p)} ((\mathbf{r}^d - \mathbf{r}) : \mathbf{n}) \quad (8)$$

where A_0 is a nonnegative model constant and f_C is a nonnegative function related to the effect of mean effective stress p . Concurrently, during dilation, the D takes the following form:

$$D = A_0 \frac{f_D(\theta)}{h_{\text{post-liq}} h_{\text{fd}}} ((\mathbf{r}^d - \mathbf{r}) : \mathbf{n}) \quad (9)$$

where A_0 is the same nonnegative model constant as in Equation 8 and f_D a non-negative function of Lode angle θ . Function h_{fd} introduces fabric evolution effects on the dilatancy D in dilation via:

$$h_{\text{fd}} = 1 + \langle f_{\text{pd}} - c_{\text{fd}} \rangle \quad (10)$$

where $c_{\text{fd}} = 3$ is a fixed model constant and f_{pd} is a cumulative index which increases gradually in a manner similar to Equation 5 for f_p , but only with positive plastic volumetric strain (i.e., only during contraction). This gradual increase of h_{fd} leads to an ever-decreasing tendency for dilation, especially when volume change is significant (e.g., in cases of fully drained conditions). Finally, the function $h_{\text{post-liq}}$ takes values larger than 1 only after initial liquefaction, i.e., only after $p < p_1$ for the first time with $p_1 = \min(0.05p_0, 10 \text{ kPa})$. This function accounts phenomenologically for post-liquefaction accumulation of strains by decreasing the dilatancy D during dilation. It is given by:

$$h_{\text{post-liq}} = 1 + \left(2^{f_E(p)} - 1 \right) f_1 \quad (11)$$

where f_1 is a cumulative fabric-based index, activated once initial liquefaction occurs. The f_1 constantly increases thereafter, as a function of the absolute value of the plastic volumetric strain, and its rate of increase is quantified via model constant L_0 . Exponent $f_E(p)$ is a nonnegative function of p with an upper limit of 1.0 (when the p approaches zero) and a lower limit of 0.0 (when the p has sufficiently increased far from the liquefaction regime). Its role is to degrade the value of $h_{\text{post-liq}}$ back to 1.0, when the stress state has moved far from $p \approx 0$ regime, regardless of the f_1 value.

Due to the inclusion of tensor \mathbf{r}_{ini} in multiple constitutive parts (e.g., Equations 2, 3, 8), this model is subject to the problem of stress-strain overshooting upon unloading and immediate reloading, i.e., the estimation of an unrealistic stress-strain curve that overshoots the expected stress-strain curve that would appear, if this unloading-reloading cycle had not occurred. This is remedied by “adjusting” the value of \mathbf{r}_{ini} depending on the loading history. Here, the problem is addressed in a two-step procedure. The first step is to check whether a detected load reversal is “formal” or “informal”: when a load reversal is detected for the initiation of load path $(m+1)$, say at $\mathbf{r} = \mathbf{r}^{(m)}$, it is considered by default “informal” and no update of \mathbf{r}_{ini} is performed. This holds until the stress-ratio change from the “informal” load reversal point is larger than a (small) tolerance level $r_{\text{tol}} (= 0.01 \text{ here})$, i.e., when:

$$\sqrt{\left(\frac{2}{3}\right)\left(r - r^{(m)}\right) : \left(r - r^{(m)}\right)} \geq r_{tol} \quad (12)$$

If Equation 12 holds true, then the load reversal point is considered “*formal*” and the “*appropriate*” value of r_{ini} to be used in the upcoming load path (m+1) is established on the basis of the robust criterion proposed by Dafalias and Taiebat (2016) according to which:

$$r_{ini}^{(m+1)} = k r_{ini}^{(m-1)} + (1 - k) r^{(m)} \quad (13)$$

where $r_{ini}^{(m-1)}$ is the r_{ini} value of the previous loading path that has been kept in memory and k is a weighting factor ($0.0 \leq k \leq 1.0$) on the basis of the plastic deviatoric strain developed during the ongoing path to an explicitly pre-defined constant threshold value ($= 10^{-4}$ here). As shown in Figure 3 in simulations of the (deviatoric) stress q_{TX} ($= \sigma_a - \sigma_r$) versus the (axial) strain ε_a response of an undrained triaxial test, employing only the second criterion (Eq. 13) is sufficient to mitigate overshooting due to one “*informal*” small unload-reload cycle (subplot b). However, both criteria (Eqs. 12 and 13) are necessary when numerous successive small unload-reload cycles (quite common in dynamic problems) are applied (subplot c).

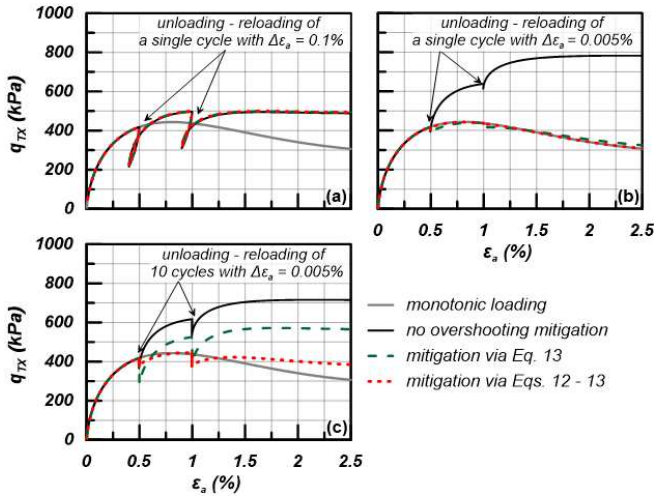


Figure 3. Performance of different schemes to treat overshooting for the stress–strain response of an undrained triaxial compression test, with three different cases of unloading–reloading cycles.

3 MODEL PERFORMANCE

In this section, the performance of the *LiPa* model is evaluated at the element test level. The validation includes simulations of both monotonic and cyclic shearing tests on two granular soils: Toyoura sand ($D_{50} \approx 0.16$ mm) and Pea gravels ($D_{50} \approx 9$ mm). In Limnaiou and Papadimitriou (2022, 2023a, 2023b) additional validation plots are presented for other sands, like Ottawa-F65 ($D_{50} = 0.20$ mm), Nevada ($D_{50} = 0.10$ mm) and Monterey ($D_{50} = 0.37$ mm), as well as the step-by-step calibration procedure of all 14 model constants. Based on these

publications, as well as the list for Toyoura sand in Table 1, it is deduced that for sands the model is proposed with a unique set of sand-specific constants for both monotonic and cyclic shearing. For gravels, there are much fewer published data. At least for the Pea gravels in Table 1, it is shown that only the fabric-related model constant N_o needs to be deactivated (set to zero) in case of monotonic loading, while maintaining all other model constants the same as for cyclic loading. In cases that cyclic loading follows monotonic loading or the opposite, each loading phase may be simulated with the appropriate N_o value while keeping all other model constants the same.

Table 1. Model constants for Toyoura sand and Pea gravels

Constitutive part	Parameter	Values	
		Toyourea sand	Pea gravels
Elasticity	G_o	650	580
	ν	0.15	0.05
	e_{ref}	0.934	0.72
	λ	0.019	0.019
CSL	ξ	0.70	2
	M_c^c	1.25	1.1
	c	0.712	0.74
Plastic modulus	n^b	1.1	0.05
	h_o	60	300
Dilatancy	ch	12	0.5
	n^d	2	1
	A_o	1.5	1.5
Fabric	N_o	1550	6250 (cyclic) 0 (monotonic)
	Post-liquefaction	L_o	2500

Figure 4 show one-to-one comparisons of model simulations to the respective experimental data for undrained monotonic triaxial compression tests (TX) on isotropically consolidated specimens of Toyoura sand (Verdugo and Ishihara, 1996). The comparison is shown in terms of stress-strain relations ($q_{TX} - \varepsilon_a$ in Figure 4a) and effective stress paths ($q_{TX} - p$ in Figure 4b). In these tests, a huge variability of initial conditions is explored: $e_o = 0.735 - 0.833$ ($D_r = 37\% - 63\%$) and initial $p_o = 100 - 1000$ kPa. The figure depicts the versatility of the model to simulate both contractive and dilative response depending on the combination of e_o and p_o . On the lower part of the plot, Figures 4c and 4d compare the model simulations to the respective experimental data from undrained monotonic simple shear (SS) tests, performed on dense ($e_o = 0.592 - 0.598$, $D_r \approx 87\% - 90\%$) specimens of Pea gravels (Hubler et al. 2017). The comparison of data versus simulations is shown in terms of (shear) stress-strain relations ($\tau - \gamma_{SS}$ in Figure 4c) and the effective stress path ($\tau - \sigma_a$ in Figure 4d). The simulations refer to three levels of initial axial effective

stresses, $\sigma_a = 100, 200$ and 400 kPa. The model simulations can be evaluated as quite satisfactory compared to the data, especially for the higher stress level.

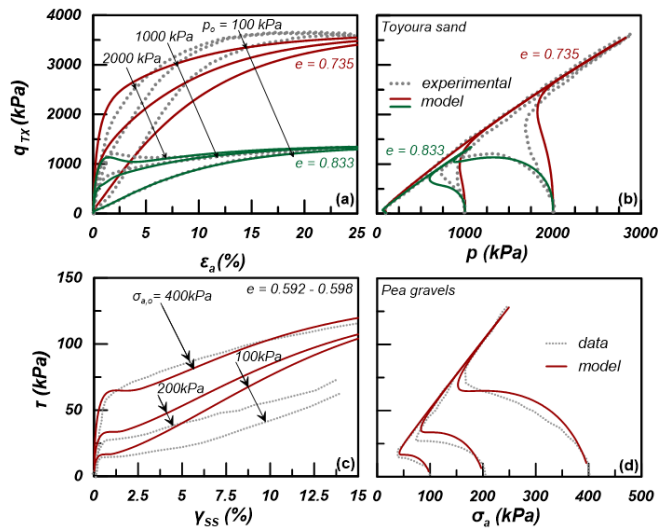


Figure 4. Experimental results and model simulations of undrained monotonic tests: a, b: TX tests on Toyoura sand; c, d: SS tests on Pea gravels

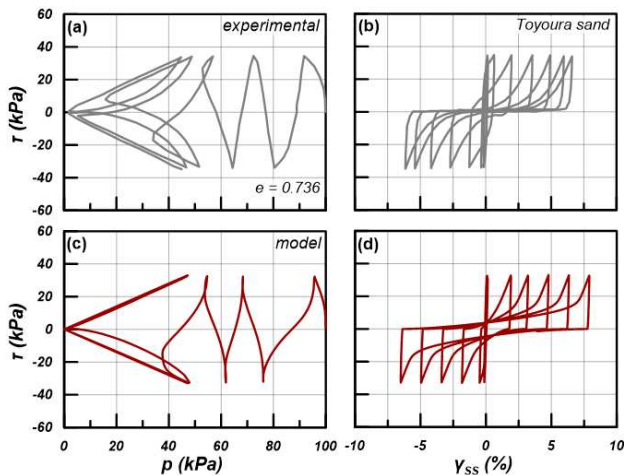


Figure 5. Experimental results and model simulations of an undrained cyclic torsional shear test on Toyoura sand

Figure 5 shows the model's capability in simulating an undrained cyclic torsional shear (TS) test conducted on Toyoura sand (Zhang, 1997), as an example. It was isotropically consolidated at $p_0 = 100$ kPa and a void ratio $e_0 = 0.736$ ($D_r = 70\%$). The single amplitude of the cyclically applied shear stress for this test is $\tau_{cyc} = 33$ kPa. The comparison is made in terms of the effective stress path ($\tau - p$ in Figures 5a, c) and the (shear) stress-strain relation ($\tau - \gamma_{SS}$ in Figures 5b, d). The comparison is quite satisfactory with the model successfully capturing the number of cycles to liquefaction, the cyclic mobility response and the strain accumulation with cycles after liquefaction triggering.

However, the accuracy in simulating liquefaction response cannot be fully assessed by one-to-one comparisons in the form of Figure 5. This is better achieved by summary comparisons in terms of liquefaction resistance curves. To this end, the model's accuracy is

evaluated through comparison with a group of liquefaction resistance curves for Toyoura sand (as denoted in the figure), instead of a single set of curves. Only in this way one may account for the plethora of the data in the pertinent literature and their pertinent scatter. This comparison is presented in Figure 6, on the basis of cyclic triaxial tests and simulations for Toyoura sand. The grouping of the experimental data was based on the relative density D_r of the sand, in groups of test data with $D_r = 40\%$ (red symbols; $e = 0.811$), 60% (green symbols; $e = 0.756$) and 87.5% (black symbols; $e = 0.691$). All selected literature liquefaction resistance curves refer to isotropically consolidated samples at initial mean effective stress $p_0 = 100$ kPa. The comparison is made in terms of cyclic stress ratio $CSR (= q_{TX,cyc}/2p_0)$ versus N_i , i.e., the number of cycles required for a double amplitude axial strain equal to 5% to be developed. The liquefaction resistance curves procuring from the simulations generally plot within the range of the experimental data and depict properly the increase in liquefaction resistance with relative density.

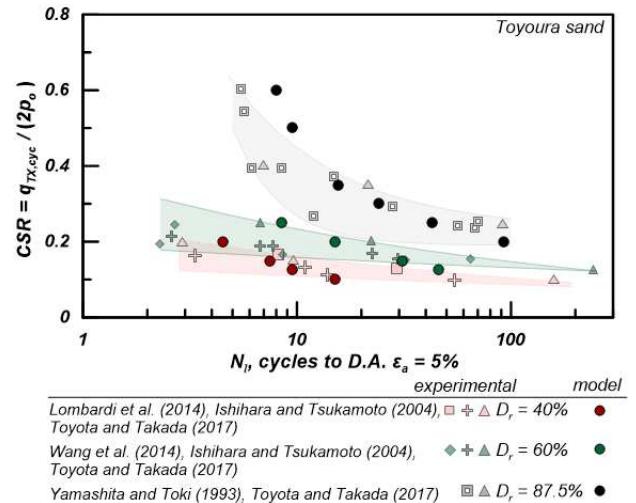


Figure 6. Experimental results and model simulations of liquefaction resistance curves, based on undrained cyclic TX tests on Toyoura sand at different D_r values ($p_0 = 100$ kPa)

Finally, Figure 7 presents a summary comparison of accumulated volumetric strains ε_{vol} (Figure 7a) and accumulated shear strains $\gamma_{TX} = \varepsilon_a - \varepsilon_r$ (Figure 7b) in cyclic drained triaxial tests as simulated by the new model vs the pertinent values from the empirical relations of Bouckovalas et al. (1988) and Stamatopoulos et al. (1991). Strain accumulation is measured after $N_d = 1, 30, 100$ and 300 cycles, as examples. The simulations are performed for Toyoura sand and for initial relative densities of $D_r = 40\%$, 60% and 80% (with initial void ratios $e_0 = 0.829, 0.756$ and 0.683). All simulated tests were anisotropically consolidated at a mean effective stress $p_0 = 200$ kPa and values of $K_0 = 0.50$ and 0.716 . The anisotropic consolidation permits studying the accumulation of both volumetric ε_{vol} and shear γ_{TX} strains with cycles under drained loading. Different colors depict different number of cycles, while the solid diagonal

line is the locus of points of perfect agreement between simulations by the model and predictions by the empirical relations. Similarly, the two dashed lines define the loci of overestimation and underestimation by the denoted factor. In terms of volumetric strains ε_{vol} (Figure 7a), a quite good agreement is observed, as the ratio of simulated over empirical values ranges between 0.5 and 2. On the other hand, in terms of accumulated shear strains γ_{TX} (Figure 7b), the comparison is less impressive, but remains satisfactory (ratio $\approx 0.33 - 3$).

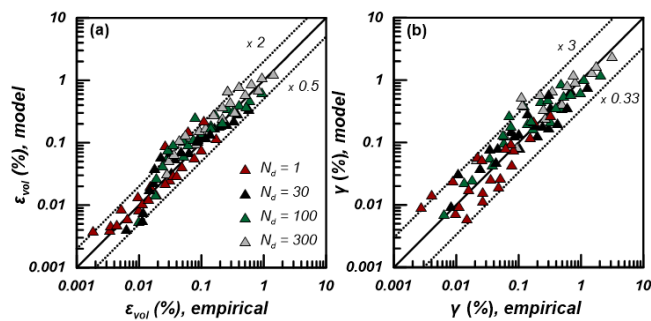


Figure 7 Comparison of accumulated strains after $N_d = 1, 30, 100$ and 300 cycles of drained triaxial tests on Toyoura sand, as simulated by the model versus the empirically predicted values: a) volumetric strains, b) shear strains.

4 CONCLUSIONS

This paper presents the outline of a new SANISAND-type bounding surface plasticity model with reversal surfaces named *LiPa*. It is a general-purpose model with 14 constants. Novel constitutive ingredients include fabric-related variables affecting the plastic modulus and the dilatancy function aiming at accurate strain accumulation with cycles under drained and undrained shearing, a dilatancy-reducing variable for accurate post-liquefaction strain accumulation and an enhanced scheme for avoiding stress-strain overshooting.

As a whole, the model is proven capable of providing accurate simulations of both the monotonic response (until the critical state) and the cyclic response (for any shear strain level) of granular soils, irrespective of initial density and mean effective stress level. This accuracy is attained with a single set of model constants for sands. For gravels, the (so far limited) experience shows that only the fabric-related model constant N_0 needs to be set to zero in case of monotonic loading.

5 ACKNOWLEDGEMENTS

This paper was supported by the Onassis Foundation Scholarship ID: G ZO 013–1/2018-2019, awarded to the first author for her Ph.D. studies.

6 REFERENCES

Andrianopoulos, K.I., Papadimitriou, A.G., Bouckovalas,

- G.D. 2010. Bounding surface plasticity model for the seismic liquefaction analysis of geotechnical structures. *Soil Dyn Earthq Eng* **30**, 895-911.
- Been, K., Jefferies, M.G. 1985. A state parameter for sands. *Geotechnique* **35**, 99-112.
- Bouckovalas, G., Whitman, R.V., Marr, W.A. 1984. Permanent Displacement of Sand with Cyclic Loading, *Jour of Geotechn Eng* **110(11)**, 1606-1623.
- Dafalias, Y.F., Manzari, M.T. 2004. Simple plasticity sand model accounting for fabric change effects. *Jour of Eng. Mech.*, **130**, 6, 622-634.
- Dafalias, Y.F., Taiebat, M. 2016. SANISAND-Z: zero elastic range sand plasticity model, *Geotechnique* **66**, 999-1013.
- Hubler, J. F., Athanasopoulos-Zekkos, A., Zekkos, D. 2017. Monotonic, Cyclic, and Postcyclic Simple Shear Response of Three Uniform Gravels in Constant Volume Conditions, *Jour. Geotechn and Geoenv Eng* **143(9)**, 04017043.
- Ishihara, K., Tsukamoto, Y. 2004. Cyclic strength of imperfectly saturated sands and analysis of liquefaction, *Proc. Japan Acad.*, **80(8)**, 372–391.
- Limnaiou, T.G., Papadimitriou, A.G. 2022. Verification of bounding surface plasticity model with reversal surfaces for the analysis of liquefaction problems, *Soil Dyn Earthq Eng* **163**, 107394.
- Limnaiou, T.G., Papadimitriou, A.G. 2023a. Bounding surface plasticity model with reversal surfaces for the monotonic and cyclic shearing of sands, *Acta Geotech* **18**, 235-263.
- Limnaiou, T.G., Papadimitriou, A.G. 2023b. Validation of a new constitutive model with reversal surfaces for the analysis of liquefaction-induced phenomena. *Proceedings, 10th Europ Conf on NUMGE* (Eds: Zdravković, L., Kontoe, S., Taborda, D.M.G. & Tsiampousi, A.) Imperial College, London.
- Lombardi, D., Bhattacharya, S., Hyodo, M., Kaneko, T. 2014. Undrained behaviour of two silica sands and practical implications for modelling SSI in liquefiable soils. *Soil Dyn Earthq Eng* **66**, 293–304.
- Manzari, M.T., Dafalias, Y.F. 1997. A critical state two-surface plasticity model for sands, *Geotechnique* **47**, 255-272.
- Papadimitriou, A.G., Chaloulos, Y.K., Dafalias, Y.F. 2019. A fabric-based sand plasticity model with reversal surfaces within anisotropic critical state theory. *Acta Geotech* **14**, 253-277.
- Stamatopoulos, C. A., Bouckovalas, G., Whitman, R. V. 1991. Analytical Prediction of Earthquake-Induced Permanent Deformations. *Journ Geotechn Eng* **117(10)**, 1471-1491.
- Toyota, H., Takada, S. 2017. Variation of Liquefaction Strength Induced by Monotonic and Cyclic Loading Histories. *Jour. Geotechn and Geoenv Eng* **143(4)**
- Wang, H., Koseki, J., Sato, T. 2014. Resistance against liquefaction of unsaturated Toyoura sand and Inagi sand. *Bulletin of ERS*, **47**.
- Verdugo, R., Ishihara, K. 1996. The Steady State of Sandy Soils. *Soils and Foundations* **36(2)**, 81–91.
- Yamashita, S., Toki, S. 1993. Effects of Fabric Anisotropy of Sand on Cyclic Undrained Triaxial and Torsional Strengths. *Soils and Foundations* **33(3)**, 92–104
- Zhang, J.M. 1997. Cyclic critical stress state theory of sand with its application to geotechnical problems. PhD Thesis. Tokyo Institute of Technology.